

A Coordinated X-ray and Optical Campaign on the Nearest Massive Eclipsing Binary, δ Ori Aa. I. Overview of the X-ray Spectrum

M. F. Corcoran^{1,2}, J. S. Nichols³, H. Pablo⁴, T. Shenar⁵, A. M. T. Pollock⁶,
W. L. Waldron⁷, A. F. J. Moffat⁴, N. D. Richardson⁴, C. M. P. Russell⁸, K. Hamaguchi^{1,9},
D. P. Huenemoerder¹⁰, L. Oskina⁵, W.-R. Hamann⁵, Y. Nazé^{11,23}, R. Ignace¹²,
N. R. Evans¹³, J. R. Lomax¹⁴, J. L. Hoffman¹⁵, K. Gayley¹⁶, S. P. Owocki¹⁷,
M. Leutenegger^{1,9}, T. R. Gull¹⁸, K. T. Hole¹⁹, J. Lauer³, & R. C. Iping^{20,21}

ABSTRACT

We present an overview of four deep phase-constrained *Chandra* HETGS X-ray observations of δ Ori A. Delta Ori A is actually a triple system which includes the nearest massive eclipsing spectroscopic binary, δ Ori Aa, the only such object that can be observed with little phase-smearing with the *Chandra* gratings. Since the fainter star, δ Ori Aa2, has a much lower X-ray luminosity than the brighter primary (δ Ori Aa1), δ Ori Aa provides a unique system with which to test the spatial distribution of the X-ray emitting gas around δ Ori Aa1 via occultation by the photosphere of, and wind cavity around, the X-ray dark secondary. Here we discuss the X-ray spectrum and X-ray line profiles for the combined observation, having an exposure time of nearly 500 ks and covering nearly the entire binary orbit. The companion papers discuss the X-ray variability seen in the *Chandra* spectra, present new space-based photometry and ground-based radial velocities obtained simultaneous with the X-ray data to better constrain the system parameters, and model the effects of X-rays on the optical and UV spectra. We find that the X-ray emission is dominated by embedded wind shock emission from star Aa1, with little contribution from the tertiary star Ab or the shocked gas produced by the collision of the wind of Aa1 against the surface of Aa2. We find a similar temperature distribution to previous X-ray spectrum analyses. We also show that the line half-widths are about 0.3 – 0.5 times the terminal velocity of the wind of star Aa1. We find a strong anti-correlation between line widths and the line excitation energy, which suggests that longer-wavelength, lower-temperature lines form farther out in the wind. Our analysis also indicates that the ratio of the intensities of the strong and weak lines of Fe XVII and Ne X are inconsistent with model predictions, which may be an effect of resonance scattering.

Subject headings: stars: individual (δ Ori A) — binaries: close — binaries: eclipsing — stars: early-type — stars: mass-loss — X-rays: stars

¹CRESST and X-ray Astrophysics Laboratory, NASA/Goddard Space Flight Center, Greenbelt, MD 20771, USA

²Universities Space Research Association, 7178 Columbia Gateway Dr. Columbia, MD 21046, USA

³Harvard-Smithsonian Center for Astrophysics, 60 Garden Street, MS 34, Cambridge, MA 02138, USA

⁴Département de physique and Centre de Recherche

en Astrophysique du Québec (CRAQ), Université de Montréal, C.P. 6128, Succ. Centre-Ville, Montréal, Québec, H3C 3J7, Canada

⁵Institut für Physik und Astronomie, Universität Potsdam, Karl-Liebknecht-Str. 24/25, D-14476 Potsdam, Germany

⁶European Space Agency, *XMM-Newton* Science Operations Centre, European Space Astronomy Centre, Apartado 78, E-28691 Villanueva de la Cañada, Spain

1. Introduction

Massive O-type stars, though rare, are a primary drivers of the chemical, ionization, and pressure evolution of the interstellar medium. The evolution of these stars from the main sequence to supernova depends on their mass and is significantly affected by stellar wind mass-loss. Our best estimates of mass, radius, and luminosity for O stars come from direct dynamical analyses of photometric and radial velocity variations in massive, eclipsing binaries. However, because massive stars are rare and massive binaries which have been studied in detail rarer still (of the 2386 systems listed in the Ninth Catalog of Spectroscopic Binaries, only 82 of them have O-type components), direct dynamical determinations of stellar param-

eters are only known for a few systems.

Current uncertainties regarding the amount and distribution of mass lost through stellar winds are even larger, since it is difficult to determine stellar wind parameters in a direct, model-independent way. Radiatively driven stellar winds have mass-loss rates of $\dot{M} \sim 10^{-5} - 10^{-7} M_{\odot} \text{yr}^{-1}$ (for a review, see Kudritzki & Puls 2000). However, observationally determined mass-loss rates have been estimated, in many, if not most cases, using an idealized smooth, spherically symmetric wind. Stellar winds are probably not spherical; variations of photospheric temperature with latitude are inevitable because of stellar rotation (and tidal deformation of stars in binaries), and these temperature variations will produce latitudinally dependent wind densities and velocities (Owocki et al. 1996). Stellar winds are not smooth either; the radiative driving force is inherently unstable to small velocity perturbations, and wind instabilities are expected to grow into dense structures (clumps) distributed through the wind. In addition, clumps can also be produced by sub-surface convective zones in massive stars caused by opacity peaks associated with the ionization state of helium and iron (Cantiello et al. 2009). Wind clumps play an important role in determining the overall mass-loss rate, since they carry most of the mass but occupy little volume. An outstanding question is to determine the number and mass/spatial distribution of embedded wind clumps.

Collisions between clumps, or between clumps and ambient wind material at high differential velocities can produce pockets of hot shocked gas embedded in the wind. Given wind speeds of up to thousands of kilometers per second, these embedded wind shocks should generate observable X-ray emission (as originally proposed by Lucy & White 1980). There have been efforts to determine the fraction of the wind that is clumped, and the radial distribution of the embedded wind shocks, through analysis of the X-ray radiation they produce. High spectral resolution X-ray grating spectrometry provides a unique tool to determine the properties of the X-ray emitting hot shocked gas produced by embedded wind clumps. In particular, the forbidden-to-intercombination (f/i) line ratios of strong He-like transitions, and analysis of profiles of H-like ions and other strong

⁷Eureka Scientific, Inc., 2452 Delmer St., Oakland, CA 94602, USA

⁸NASA-GSFC, Code 662, Goddard Space Flight Center, Greenbelt, MD, 20771 USA

⁹Department of Physics, University of Maryland, Baltimore County, 1000 Hilltop Circle, Baltimore, MD 21250, USA

¹⁰Massachusetts Institute of Technology, Kavli Institute for Astrophysics and Space Research, 77 Massachusetts Avenue, Cambridge, MA 02139 USA

¹¹Groupe d'Astrophysique des Hautes Energies, Institut d'Astrophysique et de Géophysique, Université de Liège, 17, Allée du 6 Août, B5c, B-4000 Sart Tilman, Belgium

¹²Physics and Astronomy, East Tennessee State University, Johnson City, TN 37614, USA.

¹³Harvard-Smithsonian Center for Astrophysics, 60 Garden Street, MS 4, Cambridge, MA 02138, USA

¹⁴Homer L. Dodge Department of Physics and Astronomy, University of Oklahoma, 440 W Brooks Street, Norman, OK, 73019, USA

¹⁵Department of Physics and Astronomy, University of Denver, 2112 E. Wesley Avenue, Denver, CO, 80208, USA

¹⁶Department of Physics and Astronomy, University of Iowa, Iowa City, IA 52242, USA

¹⁷University of Delaware, Bartol Research Institute, Newark, DE 19716, USA

¹⁸Laboratory for Extraterrestrial Planets and Stellar Astrophysics, Code 667, NASA/Goddard Space Flight Center, Greenbelt, MD 20771, USA

¹⁹Department of Physics, Weber State University, 2508 University Circle, Ogden, UT 84408, USA

²⁰CRESSST and Observational Cosmology Laboratory, NASA/Goddard Space Flight Center, Greenbelt, MD 20771, USA

²¹Department of Astronomy, University of Maryland, 1113 Physical Sciences Complex, College Park, MD 20742-2421, USA

²²FNRS Research Associate.

lines from high resolution spectra (mostly from the *Chandra* and *XMM* grating spectrometers) indicate that significant X-ray emission exists within 1 to 2 radii of the stellar photosphere (Waldron & Cassinelli 2001; Leutenegger et al. 2006; Waldron & Cassinelli 2007). X-ray lines of strong Ly α transitions (mainly O VIII, Ne X, Mg XII, Si XIV, and S XVI) show profiles ranging from broad and asymmetric to narrow and symmetric, apparently dependent on stellar spectral type (Walborn et al. 2009). Observed line profile shapes are an important probe of the radius of the maximum X-ray emissivity, modified by absorption from the overlying, cooler, clumped wind.

Clumping-corrected mass-loss rates derived from the analysis of resolved X-ray emission lines (Oskinova et al. 2006) are generally in good agreement with predictions of line-driven wind theory, while mass-loss rates derived from analyses of resolved X-ray emission lines are lower (by a factor of a few) if clumping is not taken into account (Cohen et al. 2014). Reducing mass-loss rates by such a large factor would significantly influence our understanding of the ultimate evolution of massive stars. However, while important wind properties, such as the onset radius of clumping, the fraction of the wind that is clumped, and the radial distribution of clumps through the wind, have been indirectly inferred from detailed X-ray line analysis (Oskinova et al. 2006; Owocki & Cohen 2006; Hervé et al. 2013), to date, there have been no attempts to determine these properties directly. In this paper, we try to directly constrain the location of the X-ray emitting gas in the wind of a massive eclipsing binary, δ Ori Aa, via occultation by the companion star of the hot gas embedded in the primary’s wind.

Delta Ori (Mintaka, HD 36486, 34 Ori) is a visual triple system composed of components A, B, and C. Delta Ori A itself is composed of a massive, short period close eclipsing system δ Ori Aa, and a more distant component, δ Ori Ab, which orbits δ Ori Aa with a period of 346 years (Tokovinin et al. 2014). The inner binary, δ Ori Aa, is the nearest massive eclipsing system in the sky. It consists of a massive O9.5 II primary (star Aa1) + a fainter secondary (star Aa2, B2V-B0.5 III), in a high-inclination ($i > 67^\circ$), short period ($P = 5^d.7324$), low eccentricity ($e \approx 0.1$) orbit (Hartmann 1904; Stebbins 1915; Koch & Hrivnak 1981;

Harvin et al. 2002; Mayer et al. 2010). Because it is nearby, bright, with a high orbital inclination, δ Ori Aa is an important system since it can serve as a fundamental calibrator of the mass-radius-luminosity relation in the upper HR diagram. It is disconcerting, though, that published stellar masses for the primary star δ Ori Aa1 are different by about a factor of two (Harvin et al. 2002; Mayer et al. 2010)¹.

Delta Ori Aa is also a bright X-ray source (Long & White 1980; Snow et al. 1981; Cassinelli & Swank 1983) and is the only eclipsing short-period O-type binary system that is bright enough to be observable with the *Chandra* gratings with little phase smearing, offering the chance to study of variations of the X-ray emission line profiles as a function of the orbital phase.

Since the luminosity of the secondary, δ Ori Aa2, is less than 10% that of the primary, and since X-ray luminosity scales with stellar bolometric luminosity (Pallavicini et al. 1981; Chlebowski et al. 1989; Berghoefer et al. 1997) for stars in this mass range, it should also be less than 10% as bright in X-rays as the primary. Thus the X-ray emission from the system is dominated by the hot gas in the wind of the primary star. Therefore, occultation of different X-ray-emitting regions in the wind of δ Ori Aa1 by the photosphere and/or wind of the X-ray faint secondary, δ Ori Aa2, presents the opportunity to directly study the radial distribution of the hot shocked gas in the primary’s wind, by measuring occultation effects in X-ray line emission as a function of ionization potential and orbital phase. Since X-ray lines of different ionization potentials are believed to form at different radial distances above the primary’s surface, differential variations in the observed set of X-ray lines as a function of orbital phase allow us to probe the hot gas distribution within the primary wind’s acceleration zone, where most of the X-ray emission is believed to originate. He-like ions in the X-ray spectrum provide a complementary measure of the radial distribution of the hot gas, since these lines are sensitive to wind density and the dilute ambient UV field. This makes δ Ori Aa a unique system with which to constrain

¹Some progress has been recently made by Harmanec et al. (2013) and by Richardson et al. (2015) in disentangling lines of δ Ori Aa2 from δ Ori Aa1 and δ Ori Ab in the composite spectrum

directly the spatial distribution of X-ray emitting clumps embedded in the wind of an important O star. The main challenge, however, is the relatively small size of δ Ori Aa2 compared to the size of the X-ray emitting region, since the hot gas is expected to be distributed in a large volume throughout the stellar wind.

This paper provides an overview of the X-ray grating spectra obtained during a 479 ksec *Chandra* campaign on δ Ori Aa+Ab in 2012. The purpose of this project was to obtain high signal-to-noise observations with the *Chandra* High Energy Transmission Grating Spectrometer (HETGS; Canizares et al. 2005) of δ Ori Aa over almost an entire binary orbit, including key orbital phases, with coordinated ground-based radial velocity monitoring at H α and He I 6678 (primarily obtained by a group of amateur astronomers), and high precision, simultaneous photometry from space by the Canadian Space Agency’s Microvariability and Oscillations of Stars telescope (*MOST*, Walker et al. 2003). This paper provides an overview of the combined HETGS spectrum from our four observations, and is organized as follows. In Section 4 we present a summary of the four observations and discuss the acquisition and reduction of the data sets. Section 5 presents an analysis of the zeroth-order image of the system to constrain the X-ray contribution of δ Ori Ab to the observed X-ray emission. Section 6 presents the temperature distribution and overall properties of the strong emission lines in the combined spectrum of the four observations. Section 7 discusses the possible influence of the collision of the wind from the primary with the weak wind or photosphere of the secondary, and the influence of any such collision on the wind’s thermal and density structure. We present conclusions in Section 8. A series of companion papers presents the results of the variability analysis of the X-ray continuum and line emission (Nichols et al. 2015, in press, Paper II), the ground-based radial velocity and *MOST* space-based photometric monitoring and analysis (Pablo et al. 2015, in press, Paper III), and a complete non-LTE analysis of the spectral energy distribution of δ Ori Aa+b from optical through X-rays (Shenar et al. 2015, in press, Paper IV).

2. Stellar And System Parameters

The stellar parameters given by Harvin et al. (2002) and Mayer et al. (2010) differ significantly, and this difference has important consequences for our understanding of the evolutionary state of the system, and the influence of mass-loss and/or non-conservative mass transfer. Harvin et al. (2002) derived masses of $M_{Aa1} = 11.2M_{\odot}$ and $M_{Aa2} = 5.6M_{\odot}$ for the primary and secondary stars, making the primary significantly overluminous for its mass (or undermassive for its spectral type). The radial velocity and photometric analysis of Mayer et al. (2010) were consistent with a substantially higher mass for the primary, $M_{Aa1} = 25M_{\odot}$, after a correction for perceived contamination of the radial velocity curve by lines from δ Ori Ab. Whether the O9.5 II primary has a normal mass and radius for its spectral type is important for understanding the history of mass exchange/mass-loss from δ Ori Aa, and how this history is related to the current state of the radiatively driven wind from the primary.

An important goal of our campaign is to derive definitive stellar and system parameters for δ Ori Aa. To this end, we obtained high-precision photometry of the star with the *MOST* satellite, along with coordinated ground-based optical spectra to allow us to obtain contemporaneous light- and radial-velocity curve solutions, and to disentangle the contributions from Aa2 and/or Ab from the stellar spectrum. We also performed an analysis of the optical and archival IUE UV spectra using the non-LTE Potsdam Wolf-Rayet (PoWR) code (Gräfener et al. 2002; Hamann & Gräfener 2003). The light curve and radial velocity curve analysis is presented in Pablo et al. (2015), while the non-LTE spectral analysis is presented in Shenar et al. (2015). Table 1 summarizes these results. In this table, the values and errors on the parameters derived from the *MOST* photometry and radial velocities are given for the low-mass solution provided in Pablo et al. (2015). Note that we find better agreement between the derived stellar parameters (luminosities, masses, radii, and temperatures) and the spectral type of δ Ori Aa1 if we use the σ -Orionis cluster distance ($d = 380$ pc, Caballero & Solano 2008) for δ Ori A, rather than the smaller Hipparcos distance. Therefore, we adopt $D = 380$ pc as the

distance to δ Ori A (for a full discussion of the distance to δ Ori A, see Shenar et al. 2015). The spectral type of δ Ori Aa2 is not well constrained; Harvin et al. (2002) assign it a spectral type of B0.5 III, while Mayer et al. (2010) do not assign a spectral type due to the difficulty in identifying lines from the star. Shenar et al. (2015) assign an early-B dwarf spectral type to δ Ori Aa2 (\approx B1V).

3. Previous X-ray Observations

X-ray emission from δ Ori was first tentatively identified via sounding rocket observations (Fisher & Meyerott 1964). X-ray imaging spectrometry of δ Ori A at low or modest resolution was obtained by the *EINSTEIN* (Long & White 1980), *ROSAT* (Haberl & White 1993), and *ASCA* (Corcoran et al. 1994) X-ray observatories. Its X-ray luminosity is typically $L_x \sim 10^{31-32}$ ergs s $^{-1}$, with $L_x/L_{bol} \approx 10^{-7}$ in accord with the canonical relation for massive stars (Pallavicini et al. 1981; Chlebowski et al. 1989; Berghoefer et al. 1997). The X-ray spectrum of δ Ori A was observed at high resolution by X-ray grating spectrometers on *Chandra* in two previous observations at restricted orbital phases. An analysis of a fifty kilosecond *Chandra* HETGS spectrum from 2000 January 13 by Miller et al. (2002) revealed strong line emission from O, Ne, Mg, and Fe, along with weaker emission from higher-ionization lines like Si XIII and S XV, and unusually narrow line half-widths of ≈ 400 km s $^{-1}$. Using a simple analysis taking into account dilution of the photospheric UV field and a $1/r^2$ falloff in wind density, Miller et al. (2002) derived formation regions for the dominant He-like ions Mg XI, Ne IX, and O VII extending just above the stellar photosphere to 3–10 times the photospheric radius. An analysis of a 100 ks *Chandra* Low Energy Transmission Grating Spectrometer (LETGS; Brinkman et al. 1987) + High Resolution Camera observation from 2007 November 09 by Raassen & Pollock (2013) also showed that the Mg XI, Ne IX, and O VII emission regions extend from 2–10 stellar radius, and showed that the longer wavelength ions like N VI and C V form at substantially greater distances from the star (50–75 times the stellar radius), and that the spectrum could be modeled by a three-temperature plasma in collisional ionization equilibrium with temperatures of 0.1, 0.2, and 0.6 keV.

4. New *Chandra* Observations

A listing of the *Chandra* observations of δ Ori Aa+Ab obtained as part of this campaign is given in Table 2. These observations were obtained with the *Chandra* HETGS+ACIS-S spectrometric array. The HETGS consists of 2 sets of gratings: the Medium Resolution Grating (MEG) covering the range 2.5–26 Å and the High Resolution Grating (HEG) covering the range 1.2–15 Å; the HEG and MEG have resolving powers of $\lambda/\Delta\lambda \approx 1000$ at long wavelengths, falling to ~ 100 near 1.5 Å (Canizares et al. 2005). Four observations covering most of the orbit were obtained within a 9-day timespan to reduce any influence of orbit-to-orbit X-ray variations, for a combined exposure time of 479 ks. Table 2 lists the start and stop HJD, phases, and exposure durations for the four individual observations. Figure 1 shows the time intervals of each observation superposed on the simultaneous MOST optical light curve of δ Ori A (Pablo et al. 2015). The *Chandra* observations provide both MEG and HEG dispersed first order spectra as well as the zeroth order image. Due to spacecraft power considerations as well as background count rate issues, it was necessary to use only five ACIS CCD chips instead of six; thus, chip S5 was not used. This means that wavelengths longer than about 19 Å in the MEG plus-side dispersed spectrum and about 9.5 Å in the HEG plus-side dispersed spectrum are not available. Therefore, the strong O VII line at 21 Å was only observed in the MEG-1 order. The buildup of contaminants on the ACIS-S optical blocking filters with time further degraded the long wavelength sensitivity for all first-order spectra. Each of the four observations experienced a large variation in focal plane temperature during the observation. While a temperature-dependent calibration is applied to each observation in standard data processing, the calibration is based on a single temperature measurement taken at the end of the observation. In particular, the focal plane temperature for portions of each observation exceeded the temperature at which the temperature-dependent effects of charge transfer inefficiency (CTI) are calibrated (Grant et al. 2006). This could cause residual errors in the correction of pulse heights for those portions of the observations in the high-temperature regime.

Table 1: Stellar, Wind and System parameters for δ Ori Aa1+Aa2 from Analysis of the Optical, UV and X-ray spectra (Shenar et al. 2015) and the Solution to the MOST Light Curve and Ground-Based Radial Velocities (Pablo et al. 2015).

Parameter	Method	
	POWR Analysis ^a	light curve & RV solution ^b
$T_{\text{eff}}[\text{kK}]$ (Aa1)	29.5 ± 0.5	30 (adopted)
$T_{\text{eff}}[\text{kK}]$ (Aa2)	25.6 ± 3	$24.1^{+0.4}_{-0.7}$
$R[R_{\odot}]$ (Aa1)	16.5 ± 1	15.1
$R[R_{\odot}]$ (Aa2)	$6.5^{+2}_{-1.5}$	5.0
$M[M_{\odot}]$ (Aa1)	24^{+10}_{-8}	23.8
$M[M_{\odot}]$ (Aa2)	8.4^e	8.5
$L[\log L_{\odot}]$ (Aa1)	5.28 ± 0.05	5.20
$L[\log L_{\odot}]$ (Aa2)	4.2 ± 0.2	3.85
$v_{\infty} [\text{km s}^{-1}]$ (Aa1)	2000 ± 100	
$v_{\infty} [\text{km s}^{-1}]$ (Aa2)	1200^e	
$\log \dot{M} [M_{\odot}/\text{yr}]$ (Aa1)	-6.4 ± 0.15	
$\log \dot{M} [M_{\odot}/\text{yr}]$ (Aa2)	≤ -6.8	
E_{B-V} (ISM)	0.065 ± 0.002	
A_V (ISM)	0.201 ± 0.006	
$\log N_{\text{H}}$ (ISM)	20.65 ± 0.05	
$P[d]$		5.732436^d
E_0 (primary min, HJD)		2456277.790 ± 0.024
T_0 (periastron, HJD)		2456295.674 ± 0.062
$a[R_{\odot}]$		43.1 ± 1.7
i [deg.]		76.5 ± 0.2
ω [deg.]		141.3 ± 0.2
$\dot{\omega}$ [deg. yr ⁻¹]		1.45 ± 0.04
e		0.1133 ± 0.0003
$\gamma [\text{km s}^{-1}]$		15.5 ± 0.7
Sp. Type (Aa1)	O9.5II ^{a,c,d}	
Sp. Type (Aa2)	B1V ^a	
D [pc]	380 (adopted)	

Notes:

^aShenar et al. (2015); ^bfrom the low-mass model solution of Pablo et al. (2015);

^cMaíz Apellániz et al. (2013); ^dMayer et al. (2010); ^eAdopted assuming a spectral type of B1V.

Table 2: New *Chandra* Observations of δ Ori Aa+Ab

ObsID	Start HJD	Start Phase	End HJD	End Phase	Midpoint HJD	Midpoint Phase	ΔT Days	Exposure s	Roll deg.
14567	2456281.21	396.604	2456282.58	396.843	2456281.90	396.724	1.37	114982	345.2
14569	2456283.76	397.049	2456285.18	397.297	2456284.47	397.173	1.42	119274	343.2
14570	2456286.06	397.450	2456287.52	397.705	2456286.79	397.578	1.46	122483	83.0
14568	2456288.67	397.905	2456290.12	398.159	2456289.39	398.032	1.45	121988	332.7

Each ObsID was processed using the standard processing pipeline used in production of the *Chandra* Transmission Grating Data Archive and Catalog (TGCAT; Huenemoerder et al. 2011). Briefly, event filtering, event transformation, spectral extraction, and response generation are done with standard *Chandra* Interactive Analysis of Observations software tools (Fruscione et al. 2006) as described in detail by Huenemoerder et al. (2011). This pipeline produces standard X-ray events, spectra, responses, effective areas, aspect histograms, and light curves. We used version 4.5.5 of the Chandra Calibration Database (CALDB), along with CIAO version 4.5 & 4.6 in the analysis presented here. In order to examine variability, the data were also divided into ~ 10 ks segments, and spectra, response files, effective areas and light curves were generated for each segment. Analysis of the time-sliced data is presented in Nichols et al. (2015).

5. Analysis of the X-ray Image

The δ Ori Aa1,2 inner binary is orbited by a more distant tertiary component (δ Ori Ab) at a current projected separation of $0''.3$ with an orbital period of ≈ 346 years (Tokovinin et al. 2014). This separation is just below the spatial resolution of *Chandra*, and thus *Chandra* imaging observations allow us to spatially examine the X-ray contribution from the Ab component. Figure 2 shows unbinned zeroth-order images from our four HETGS+ACIS observations, along with the expected location of Ab and the Aa pair at the times of the *Chandra* observations in 2012.

To constrain the X-ray contribution of δ Ori Ab, we generated zeroth-order images for the four individual pointings listed in Table 2, using the Energy-Dependent Subpixel Event Repositioning (EDSER²³) method to generate images with a pixel size of $0''.125$. We generated images in 0.3–1 and 1–3 keV bands, but found no significant differences in any of the four observations when we compared the soft and hard band images. For each image, we then applied the CIAO tool SRCEXTENT to calculate the size and associated uncertainty of the photon-count source image or using the Mexican Hat Optimization algorithm²⁴.

The results of the SRCEXTENT analysis are given in Table 3. The derived major and minor axes of each image are equal and consistent with the *Chandra* point spread function, $\sim 0.3''$. The peak of the image is consistent with the location of the Aa component, and is about a factor of two farther than the Ab component. We conclude that the peak positions of the zeroth-order images in-

²³<http://cxc.harvard.edu/ciao4.4/why/acissubpix.html>

²⁴<http://cxc.harvard.edu/ciao/ahelp/srcextent.html>

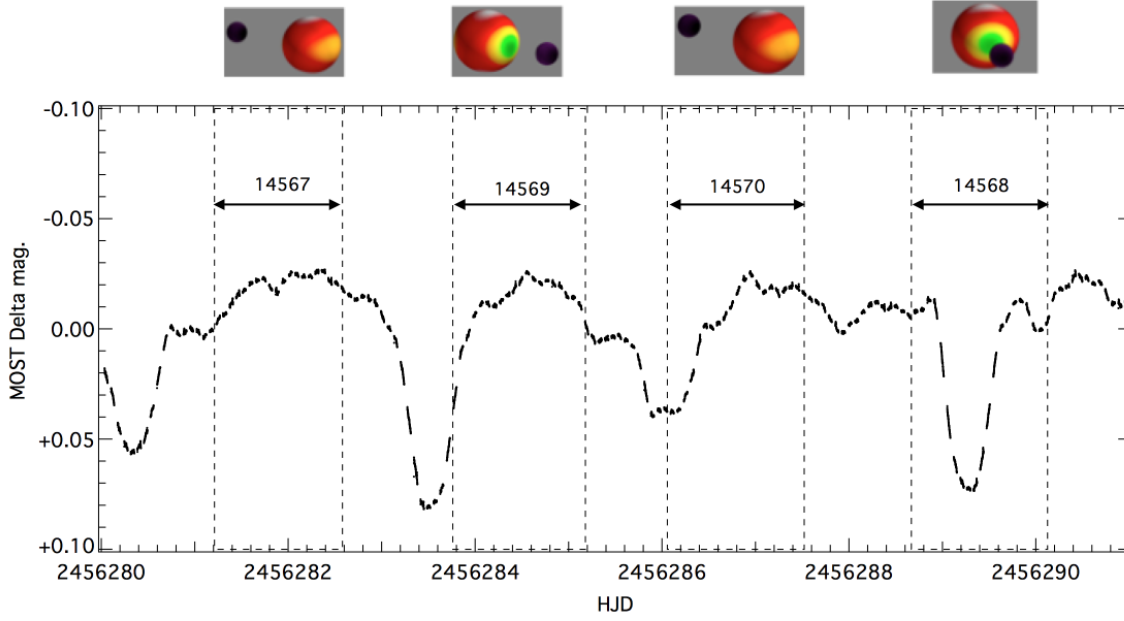


Fig. 1.— Timings of the *Chandra* observations along with the *MOST* light curve. The images above the plot show the orientations of δ Ori Aa1 and Aa2 near the midpoint of the observation according to the photometric and spectroscopic analysis of Pablo et al. (2015). In the images, the orbital angular momentum vector lies close to the plane of the paper and points to the top of the page.

dicate that Aa is the primary X-ray source, with little or no contribution from Ab. Our analysis also suggests that the ObsID 14568 image may be slightly elongated, which may indicate a possible issue with the instrumental pointing or aspect reconstruction for this observation.

6. Combined Spectrum

Figure 3 shows the co-added spectrum from the four observations, with a total exposure of 479 ks. This represents the second longest exposure yet obtained on a massive star at wavelengths $\lesssim 8 \text{ \AA}$ and a resolving power of $\lambda/\Delta\lambda > 400$. The strongest lines are O VIII, Fe XVII, Ne IX & Ne X, Mg XI & Mg XII, and Si XIII.

6.1. Temperature Distribution

We modeled the combined spectrum with a combination of absorbed collisional ionization equilibrium models using the Interactive Spectral Interpretation System (ISIS; Houck & Denicola 2000). The model we applied includes two low-temperature components seen through a common absorption component, plus a third hotter component with its own absorption component to account for any contribution from a hot colliding wind region embedded within the wind of the binary (see Section 7 below). In ISIS terminology, the mode we used was “(xaped(1) + xaped(2)) * TBabs(3) + xaped(4) * TBabs(5)”, where “xaped” represents emission from an optically thin plasma in collisional ionization equilibrium based on the ATOMDB atomic database version 2.0.2 (Smith & Brickhouse 2000; Foster et al. 2012), and “TBabs” represents interstellar absorption (Wilms et al. 2000a). Solar abundances were assumed for both the emission and absorp-

Table 3: SRCEXTENT Analysis Results

ObsID	Band keV	Major Axis arcsec	Minor Axis arcsec	PA deg.	Peak distance Aa arcsec	Peak distance Ab arcsec
14567	0.3–1	0.34	0.33	83.3	0.19	0.40
	1–3	0.32	0.28	83.8	0.19	0.42
14569	0.3–1	0.32	0.32	32.1	0.23	0.44
	1–3	0.29	0.28	27.6	0.25	0.47
14570	0.3–1	0.32	0.32	136.9	0.09	0.35
	1–3	0.26	0.22	48.3	0.08	0.34
14568	0.3–1	0.51	0.32	35.9	0.24	0.41
	1–3	0.48	0.25	31.2	0.24	0.42

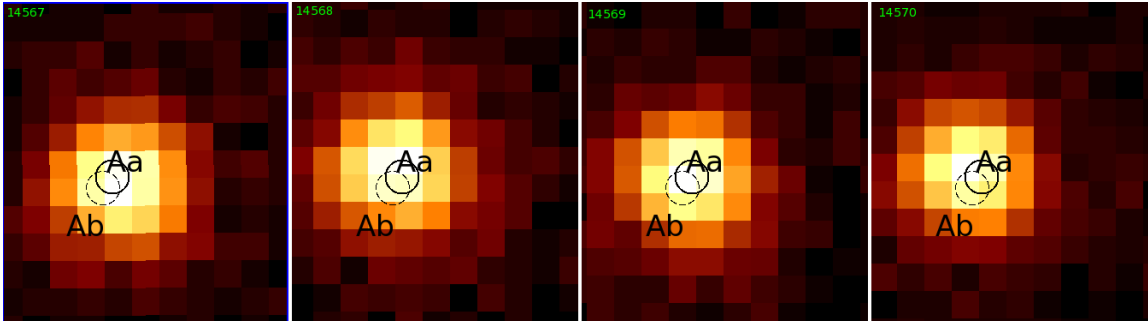


Fig. 2.— Unbinned images from the four ObsIDs listed in Table 2. ObsIDs, left to right: 14567, 14568, 14569, and 14570. The positions of Aa and Ab are shown by the full and dashed circles, respectively.

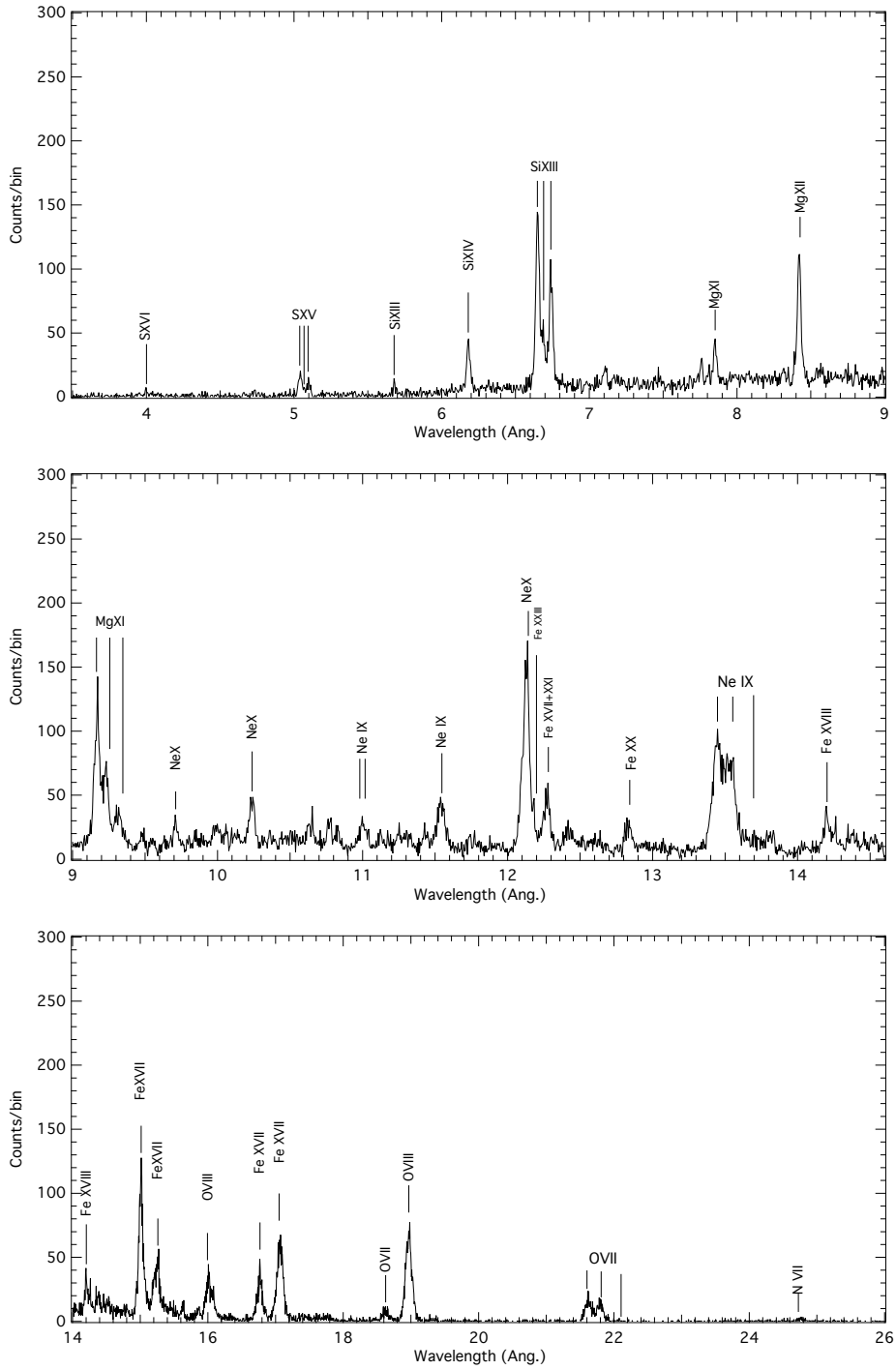


Fig. 3.— The combined MEG+HEG spectrum of δ Ori A, from 3.5 Å to 26 Å.

tion components²⁵. This model is an approximation to the actual temperature distribution and absorption, but is the simplest one we found that adequately describes the observed grating spectrum. We allowed for velocity broadening of the emission lines, with turbulent velocity broadening constrained to be less than roughly twice the maximum wind terminal velocity, 3000 km s⁻¹. We allowed the line centroid velocities of the three emission components to vary, but found that overall the line centroids are unshifted in the combined spectrum. Figure 4 compares the best-fit model to the data, while the model components are given in Table 4. In this table, we also convert the derived turbulent velocities V_{turb} to equivalent line half-widths at half maximum, using O VIII, Ne X and Mg XII for the low-, medium-, and high-temperature components, respectively.

The derived temperature distribution is similar to that found by Miller et al. (2002) in their study of the 2000 January HETGS spectrum, and by Raassen & Pollock (2013) in their analysis of an LETGS spectrum from 2007 November. In general, aside from the overall weakness of the forbidden lines compared to the model spectrum (which assumes a low-density plasma with no UV photoexcitation), the overall distribution of emission line strengths, and the continuum, are described reasonably well by the model. We note, in reality, that this three-temperature model is a simplified representation of the actual emission measure distribution with temperature. This multitemperature model mainly provides us with an adequate approximation of the local (pseudo-) continuum in order to improve line fitting and modeling.

6.2. Emission Lines

The observed X-ray emission lines in our δ Ori A spectrum provide important diagnostic information about the phase-averaged state of the hot gas within the wind of the system, and, as we show below, this is dominated by the shocked gas embedded within the wind of δ Ori Aa1, with little contribution (if any) from gas heated by the shock produced by the collision of the wind from δ Ori Aa1 with the wind or photosphere of

δ Ori Aa2. The analysis of the set of emission lines depends on choice of line profile, continuum level, and accounting for line blends.

6.2.1. Gaussian Modeling

To better account for blends and uncertainties in the continuum level, we performed a Gaussian fit to the strong lines, allowing flux, line width, and centroid velocity to vary. These fits, shown in Figure 5, were done using the three-temperature fit given in Section 6.1 above to define the continuum and amount of line blending. We set the abundance of the element to be measured to zero, with the abundances of other elements set to solar and other parameters (temperature, absorptions) fixed at the values given in Section 4. This procedure is useful to account for line blends, in particular, for the Ne X line at 12.132 Å, which is blended with an Fe XVII line at 12.124 Å. We assumed simple Gaussian line profiles for the line to be fit, and fit for both the Ly α 1 and Ly α 2 lines, with line widths and velocities fixed for both components, and the intensity ratio of the Ly α 2 to the Ly α 1 line set to the emissivity ratio at the temperature of peak emissivity. We used the Cash statistic and ISIS to perform the fits, simultaneously fitting the HEG and MEG ± 1 order spectrum from all four observations simultaneously. Table 5 shows the result of fits of the H-like Ly α lines, plus the strong Fe XVII line at 15.014 Å. In general, the Gaussian fits are poor (the reduced Cash statistic > 1.5) except for the weak Si XIV line, though the asymmetries in the bright lines are not very strong. All of the line centroids are near zero velocity, though the Ne X line is blue-shifted at about the $2\text{-}\sigma$ level.

²⁵Shenar et al. (2015) show that N and Si are slightly sub-solar, but these differences are not significant for our analysis.

Table 4: Best-Fit to the Combined HETGS spectrum. The adopted model is $(\text{APED}_1 + \text{APED}_2) * N_{H,1} + \text{APED}_3 * N_{H,2}$

Component	Parameter	Value
1	T_1 (MK)	1.25
	EM_1 (10^{55} cm^{-3})	4.46
	$V_{turb,1}$ (km s^{-1})	1313
	HWHM (km s^{-1})	1094
2	T_2 (MK)	3.33
	EM_2 (10^{55} cm^{-3})	0.87
	$V_{turb,2}$ (km s^{-1})	1143
	HWHM (km s^{-1})	953
Absorption 1	$N_{H,1}$ (10^{22} cm^{-2})	0.14
3	T_3 (MK)	9.11
	EM_3 (10^{55} cm^{-3})	0.26
	$V_{turb,3}$ (km s^{-1})	685
	HWHM (km s^{-1})	574
Absorption 2	$N_{H,2}$ (10^{22} cm^{-2})	0.24
f_x ($\text{ergs cm}^{-2} \text{ s}^{-1}$) (observed, $1.7 - 25 \text{ \AA}$)		8.2×10^{-12}
L_x (ergs s^{-1}) (observed, $1.7 - 25 \text{ \AA}$)		1.4×10^{32}
$\log L_x / L_{bol}$		-6.73
EM-weighted Average Temperature (MK)		1.94

Table 5: Gaussian Fits to the H-like lines, plus Fe XVII

	λ \AA	Flux $10^{-5} \text{ ph. s}^{-1} \text{ cm}^{-2}$	V km s^{-1}	HWHM km s^{-1}
O VIII	18.967	219^{+9}_{-10}	-9^{+37}_{-33}	918^{+38}_{-29}
Fe XVII	15.014	76^{+4}_{-3}	-24^{+42}_{-35}	971^{+53}_{-27}
Ne X	12.132	10^{+1}_{-1}	-102^{+50}_{-42}	726^{+48}_{-58}
Mg XII	8.419	1^{+0}_{-0}	-12^{+33}_{-55}	547^{+58}_{-61}
Si XIV	6.180	$0.35^{+0.05}_{-0.05}$	-49^{+45}_{-134}	544^{+116}_{-124}

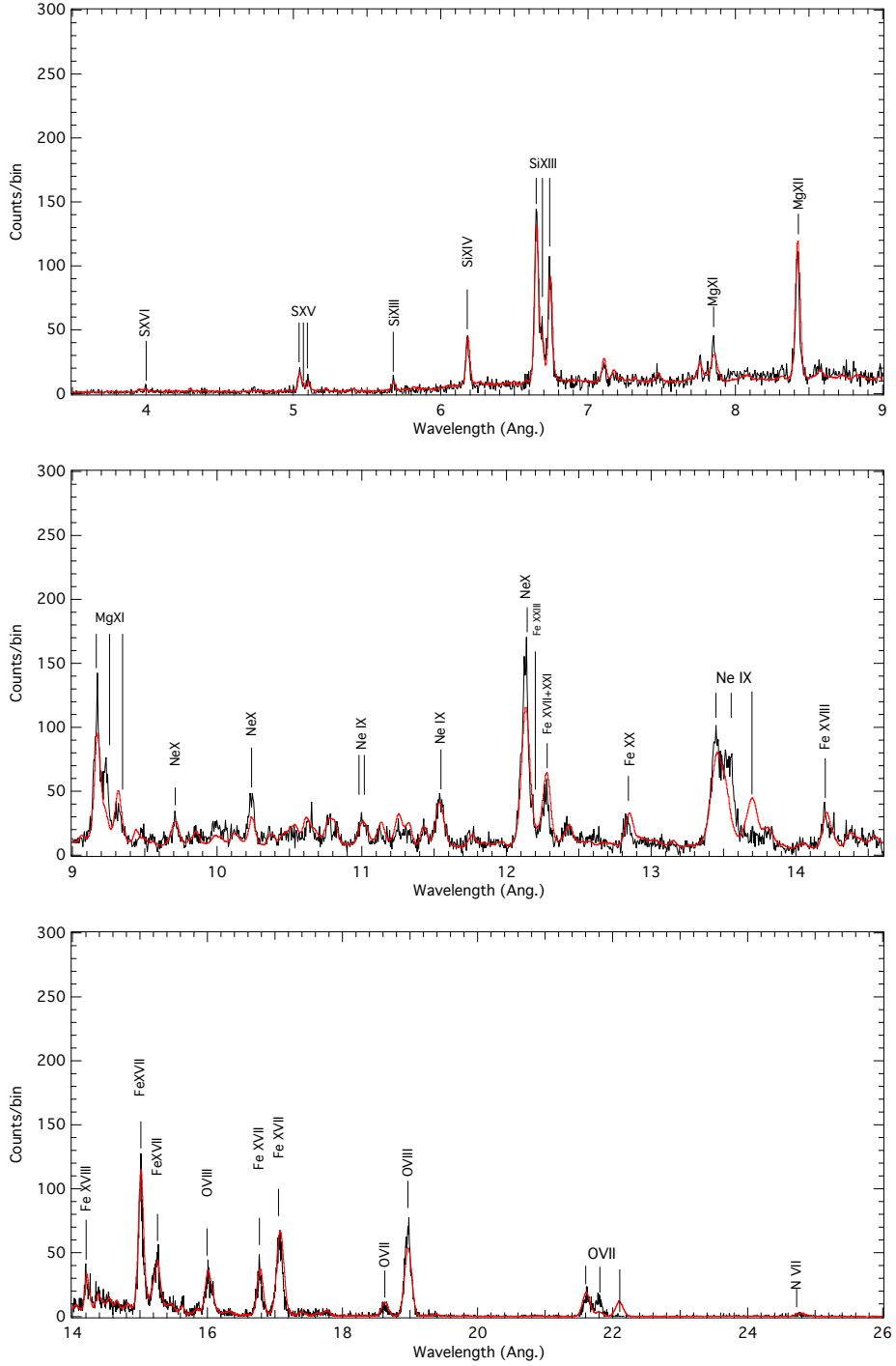


Fig. 4.— The combined MEG+HEG spectrum of δ Ori A (in black) with the 3-component fit (shown in red) given in Table 4. The model spectra, which assume low density and do not include effects of UV photoexcitation, generally overestimate the strength of the forbidden lines and underestimate the strengths of the intercombination lines, especially at longer wavelengths, most notably at O VII.

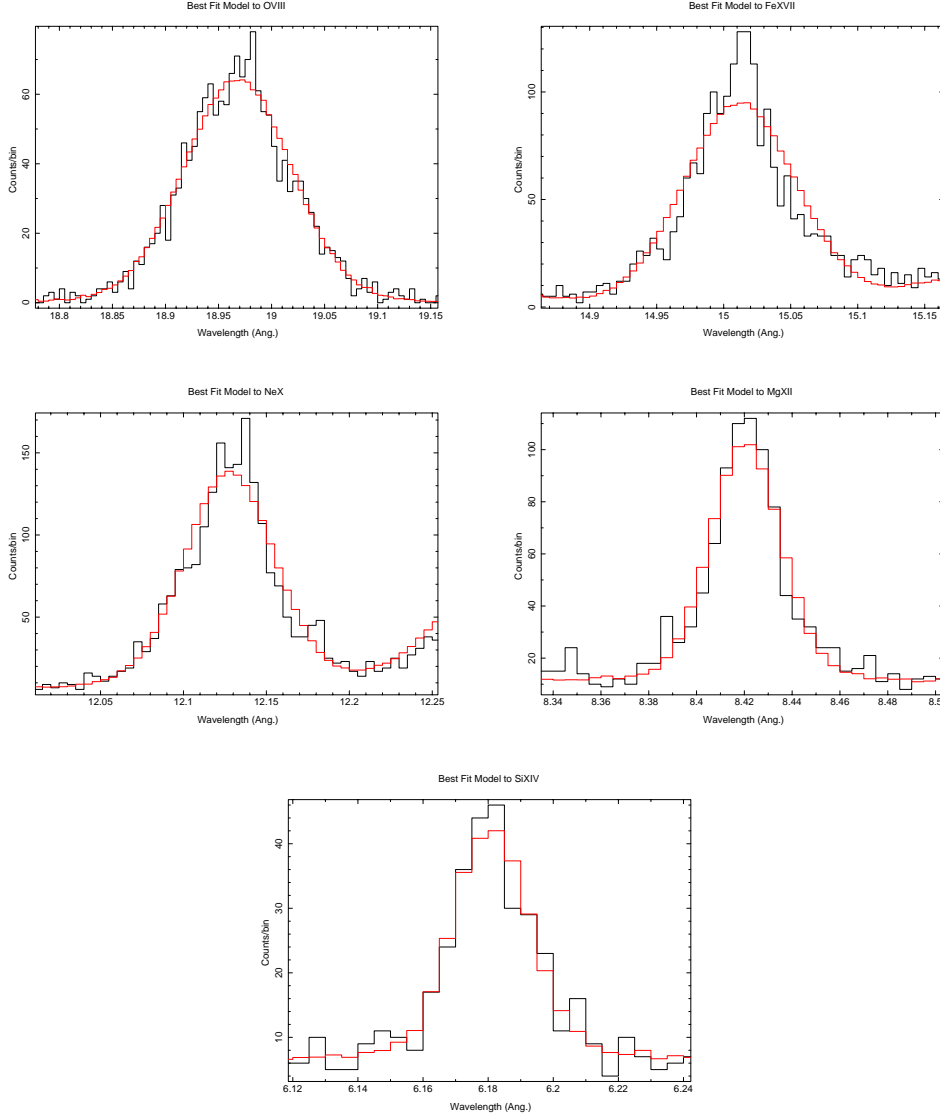


Fig. 5.— Top to bottom, left to right: O VIII; Fe XVII; Ne X; Mg XII; and Si XIV. The lines are plotted in the velocity range of -3000 km s^{-1} to $+3000 \text{ km s}^{-1}$. The best-fit Gaussian profile, and the continuum derived from the model parameters given in Table 4 is shown in red. Note that while most of the Ly α lines are adequately described by a symmetric Gaussian, the Fe XVII and Ne X lines are not as well fit by simple Gaussian profiles as the other lines. This may be due to the effects of non-uniform X-ray line opacity, as discussed in Section 6.2.2.

We also measured the forbidden (z), intercombination ($x + y$), and resonance components (w) above continuum for each of the helium-like ions (O VII, Mg X, Ne IX, and Si XIII) by Gaussian fitting. As before, we used the three-temperature fit given in Section 6.1 above to define the local continuum near the line region. Although the individual intercombination components ($x + y$) are unresolved in the HETGS spectra for all of the He-like ions, we included a Gaussian line for the x and y lines, but restricted the centroid velocity and line widths to be the same for both the x and y components. Because the forbidden, intercombination and resonance lines can have different spatial distributions throughout the wind, we allowed the widths, centroids, and line fluxes of these lines to vary individually. The forbidden component of the O VII line is weak, and, in addition, this line was only observed in the MEG-1 spectrum arm because ACIS-S chip S5 was turned off due to spacecraft power constraints. To increase signal to noise for the O VII forbidden line, and for the weak Si XIII and S XV triplets, we included data from the 2001 HETG and 2008 LETG observations when fitting. Figure 6 shows the fits to the He-like lines, and Table 6 shows the results of this three-Gaussian component fitting, while Table 7 shows the $R = z/(x + y)$ and $G = (x + y + z)/w$ ratios.

Table 7: R and G ratios

ion	$R = z/(x + y)$	$G = (x + y + z)/w$
O VII	0.04 ± 0.01	0.94 ± 0.26
Ne IX	0.27 ± 0.10	1.44 ± 0.65
Mg XI	0.96 ± 0.36	0.95 ± 0.37
Si XIII	1.77 ± 0.18	0.90 ± 0.12
S XV	3.88 ± 2.86	0.72 ± 0.74

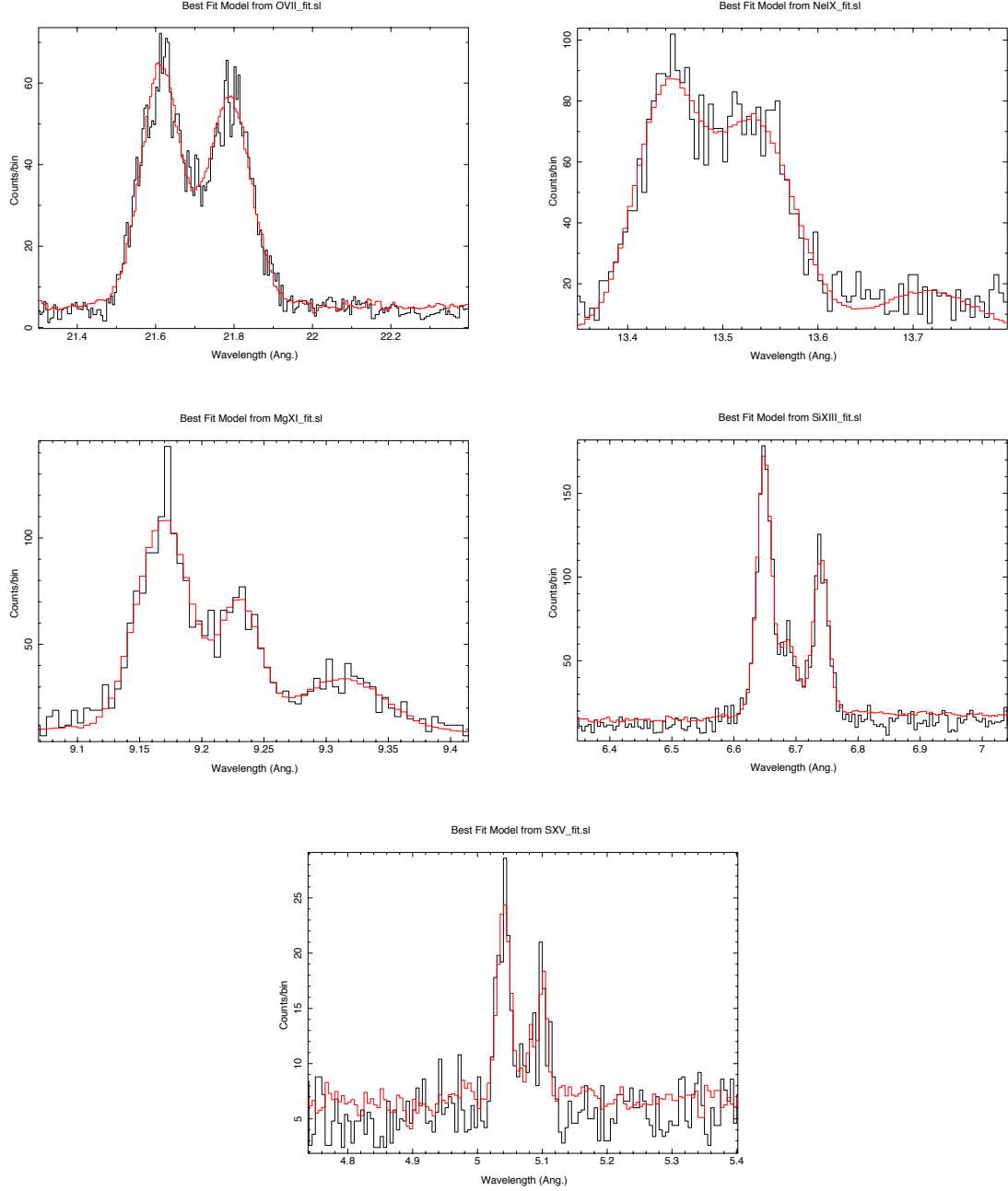


Fig. 6.— Top to bottom, left to right: O VII; Ne IX; Mg XI; Si XIII; S XV. The best fit, using a model of 4 Gaussian lines (w , x , y , & z components) and the continuum derived from the model parameters given in Table 4, is shown in red.

Table 6: Gaussian fits to the He-like lines

ion	Centroid Velocity (km s^{-1})			HWHM (km s^{-1})		
	w	$x + y$	z	w	$x + y$	z
OVII	166 ± 19	-194 ± 18	-810 ± 384	761 ± 14	826 ± 40	160 ± 270
Ne IX	-146 ± 166	-410 ± 231	441 ± 466	849 ± 138	1057 ± 222	1289 ± 49
Mg XI	8 ± 74	31 ± 109	-63 ± 270	782 ± 97	584 ± 146	1302 ± 386
Si XIII	42 ± 64	88 ± 191	-60 ± 21	488 ± 69	704 ± 361	506 ± 79
S XV	99 ± 357	1168 ± 1203	-27 ± 633	540 ± 206	966 ± 1256	69 ± 1254

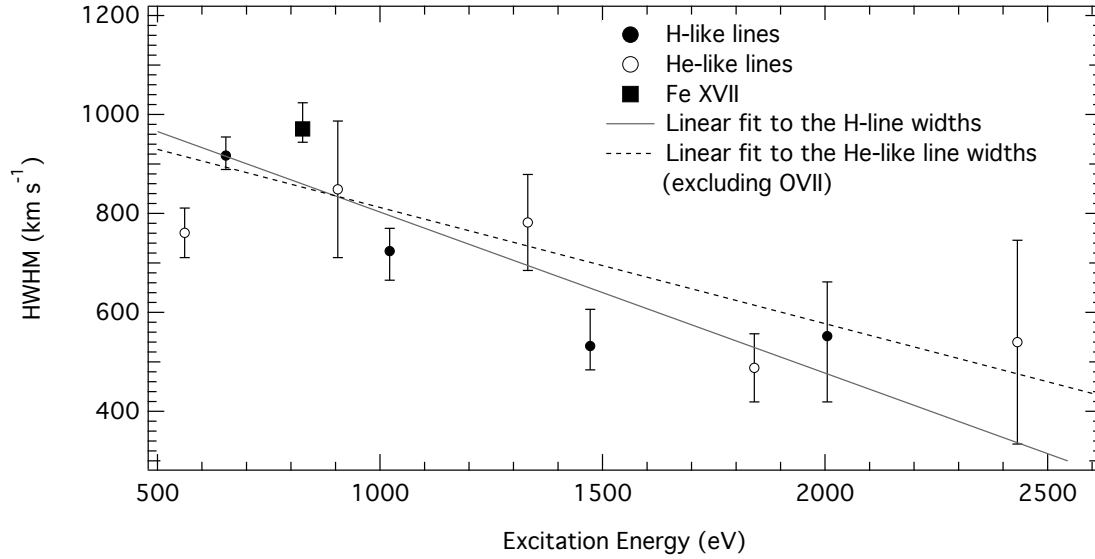


Fig. 7.— Half-widths of the H-like Ly α lines (km s^{-1}) and the He-like resonance lines versus excitation energy (eV) of the upper level of the transition. The full and dashed lines represent the best linear fit to the HWHMs from the H-like lines, and the He-like lines (excluding the O VII width), respectively.

Figure 7 shows the dependence of the half width at half maximum of the Gaussian fit versus the excitation energy of the upper level of the transition. The linear correlation coefficient for the H-like half-widths is -0.89 , indicating a strong anti-correlation between line half-width and excitation energy. For the He-like lines, the linear correlation coefficient is -0.81 , also indicating a strong anti-correlation of line half-widths and excitation energy. Thus the line widths are anti-correlated with the upper energy level, in that the line width decreases with excitation energy. This anti-correlation shows that the more highly excited lines form at lower velocities, and thus closer to the stellar surface of the primary, indicating that the higher-temperature X-ray emission emerges from deeper regions in the wind than the cooler emission.

In Figure 7, the O VII line width seems lower compared to the trend defined by the more highly excited ions. Excluding the O VII line, a linear fit to the remaining He-like lines yields a linear correlation coefficient of -0.87 , indicating a stronger anti-correlation, and also results in a steeper linear slope. This linear fit predicts that the O VII line should have a half-width of 918 eV, a factor of 1.2 larger than observed. We caution that, unlike the other lines, the O VII line was only observed in one grating order since ACIS-S chip 5 was switched off during these observations.

As a crude approximation, if we assume that the X-ray emitting material resides in a thin spherical shell at radius r around δ Ori Aa1, then the line profile will extend from $-V(r)$ to $+V(r)\sqrt{1 - (R_{Aa1}/r)^2}$, where R_{Aa1} is the radius of δ Ori Aa1, and $V(r) = V_{\infty, Aa1}(1 - R_{Aa1}/r)^\beta$, the standard velocity law for radiatively driven winds. The inverse correlation of the line widths with excitation energy suggests that the hotter X-ray emitting gas is formed over a smaller volume in the wind acceleration zone closer to the star, where wind radial velocity differentials are larger and where higher temperature shocks can be generated; cooler ions can be maintained farther out in the wind where the acceleration (and thus the velocity differential) is smaller. A similar conclusion was reached by Hervé et al. (2013) in their analysis of ζ Puppis.

6.2.2. Effects of X-ray Line Opacity

The possibility that strong resonance line photons might be scattered out of the line of sight has significant implications on our physical understanding of the X-ray emission from hot stars, especially in the interpretation of mass-loss rates derived from X-ray line profiles and abundances derived from X-ray line ratios. Resonance scattering may be important for lines with high oscillator strengths and could, in principle, change the line shape or intensity ratios, though recent analysis by Bernitt et al. (2012) suggested that our poor knowledge of the underlying atomic physics may play the dominant role in accounting for discrepancies in line intensities. Miller et al. (2002) focussed on the Fe XVII lines at 15.014 Å and 15.261 Å, which have oscillator strengths of 2.49 and 0.64, respectively. Resonance scattering might significantly affect the 15.014 Å emission line, which is one of the strongest lines in the δ Ori A X-ray spectrum, while scattering should be unimportant for the weak 15.261 Å line. Miller et al. (2002) found that the observed ratio of these two lines, as derived from their *Chandra* grating spectrum, was $I_{15.01}/I_{15.26} = 2.4 \pm 1.3$, nominally (though not significantly) below the optically thin limit $I_{15.01}/I_{15.26} = 3.5$ derived from the Smith & Brickhouse (2000) version of the Astrophysical Plasma Emission Code (APEC).

We re-examined this issue for these two Fe XVII lines using our deeper spectrum and a slightly different technique. We isolated the Fe XVII line region in the combined spectrum and fit this restricted region with an APEC-derived model, with abundances fixed at solar, including line broadening. We first fit the Fe XVII line at 15.261 Å, ignoring the region around the stronger 15.014 Å line. We then included the 15.014 Å line region and compared the predicted strength of the model 15.014 Å line to the observed line. This technique, in which we use a full thermal model to fit the spectra rather than a simple comparison of line intensities, has the benefit that line blends in the region will be more properly taken into account. We found that the model based on the best fit to the 15.261 Å line greatly overpredicted the strength of the 15.014 Å line, and can be ruled out at high confidence ($\chi^2_\nu = 3.57$, restricted to the 14.90–15.14 Å region; excluding this region, $\chi^2_\nu = 0.72$). This may be an indication of the effect

of resonance scattering on the 15.014 Å Fe XVII line. Since it appears that the 15.014 Å line is a bit narrower than the 15.261 Å line, we also re-did the fit, allowing the width of the 15.014 Å line to differ from that of the 15.261 Å line. We then re-fit only the 15.014 Å line, allowing the line broadening to vary and also allowing the normalization to vary. Figure 8 shows the resulting fit. The best-fit HWHMs for the 15.014 Å and 15.261 Å lines are 1275^{+48}_{-268} km s⁻¹ and 1496^{+109}_{-113} km s⁻¹, respectively, while the model normalizations are $0.0024^{+0.0001}_{-0.001}$ and $0.0030^{+0.001}_{-0.001}$ for the 15.014 Å and 15.261 Å lines, respectively. This analysis also shows the 15.014 Å line is significantly weaker than expected compared to the 15.261 Å line. This again may indicate that resonance scattering plays a role in determining the line profile shape and line strength, at least for the Fe XVII line, though uncertainties in the atomic models and in our definition of the temperature distribution for δ Ori A may play a significant role in altering the intensity ratios for these lines.

To further investigate the importance of resonance scattering, we also considered the Ne X lines at 10.239 Å and at 12.132 Å, which have oscillator strengths of 0.052 and 0.28, respectively. These lines complement the Fe XVII analysis since for Ne X the stronger line appears at longer wavelength; this means that any effects of differential absorption that might affect the Fe XVII line analysis would have the opposite effect on the Ne X lines. We again fit the Ne X 10.239 Å line with a single temperature APEC model, but fixed the temperature to the temperature of maximum emissivity of the Ne X lines, i.e. $T = 6.3 \times 10^6$ K. We then compared the model that best fits the Ne X 10.239 Å line to the Ne X 12.132 Å line. Note that the Ne X 12.132 Å line is blended with the Fe XXI line at 12.285 Å (which has a temperature of maximum emissivity of 12.6×10^6 K, about twice that of the Ne X line), so we restricted the Ne X 12.132 Å fitting region to the interval 12.0–12.22 Å. We again find that the model, which provides a good fit to the weaker line ($\chi^2_\nu = 0.79$), overpredicts the strength of the stronger line ($\chi^2_\nu = 8.63$), again a possible indication that resonance scattering is important in determining the flux of the strong line.

7. The Influence of Colliding Winds on the Embedded X-ray Emission

Colliding winds can have important observable effects in our analysis of the X-ray emission from δ Ori Aa in two ways. The collision of the primary wind with the surface or wind of the secondary could produce hot shocked gas which might contaminate the X-ray emission from the embedded wind shocks in the primary’s unperturbed wind. In addition, the colliding wind “bow shock” around the weaker-wind secondary produces a low-density cavity in the primary wind, and this cavity, dominated by the weak wind of δ Ori Aa2, should show little emission from embedded wind shocks. Along the line between the stars, the stellar winds will collide at the point at which their ram pressures ρv^2_\perp are equal (e.g. Stevens et al. 1992). Using the stellar, wind, and orbital parameters in Table 1, Figure 9 shows the ram pressures for Aa1 (solid) and Aa2 (dashed: apastron, dotted: periastron) assuming that the wind from each star follows the standard β velocity law, $V(r) = v_\infty(1 - R/r)^\beta$, where $V(r)$ is the wind radial velocity at a distance r from the star, R is the stellar radius, and we assume that $\beta = 0.8$ or 1.0. The ram pressure of Aa1’s wind is greater than that of Aa2 throughout the orbit, so the wind from Aa1 should directly impact Aa2’s surface, in this simple analysis.

A more thorough treatment includes the effects of Aa2’s radiation on the wind of Aa1 (and vice versa). These effects include “radiative inhibition” (Stevens & Pollock 1994) in which Aa1’s wind acceleration along the line between the stars is reduced by Aa2’s radiative force acting in opposition to the wind flow, and “sudden radiative braking” (Owocki & Gayley 1995; Gayley et al. 1997), where Aa1’s strong wind, which would otherwise impact the surface of Aa2, is suddenly decelerated by Aa2’s radiation just above the surface of Aa2. To estimate the magnitude of these effects, we solve the 1D equation of motion along the line of centers, accounting for both star’s radiative forces via the standard Castor, Abbott, and Klein (CAK) line forces (Castor et al. 1975) including the finite disk correction factor (Friend & Abbott 1986; Pauldrach et al. 1986) and gravitational acceleration. We determine the CAK parameters \bar{Q} and α (Gayley 1995) to yield the desired mass-loss rates and

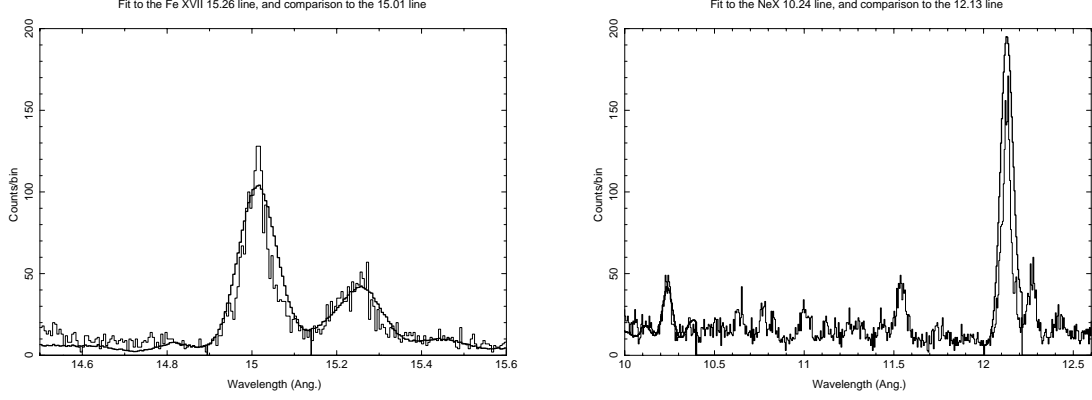


Fig. 8.— Left: APEC-based modeling of the Fe XVII 15.014 Å vs 15.261 Å lines. We first fit the 15.261 Å line by itself. The thick histogram compares that model to the observed spectrum in the 14.5–15.6 Å range. This shows that the model that fits the 15.26 Å line overpredicts the strength of the 15.01 Å line. The vertical lines from the continuum to the X-axis at 14.9 Å and 15.14 Å show the adopted wavelength range of the 15.014 Å FeXVII line. Right: APEC model fit to the Ne X 10.24 Å compared to the NeX 12.134 Å line. The model (shown by the thick histogram) that fits the weaker 10.24 Å line overpredicts the strength of the stronger 12.134 Å line.

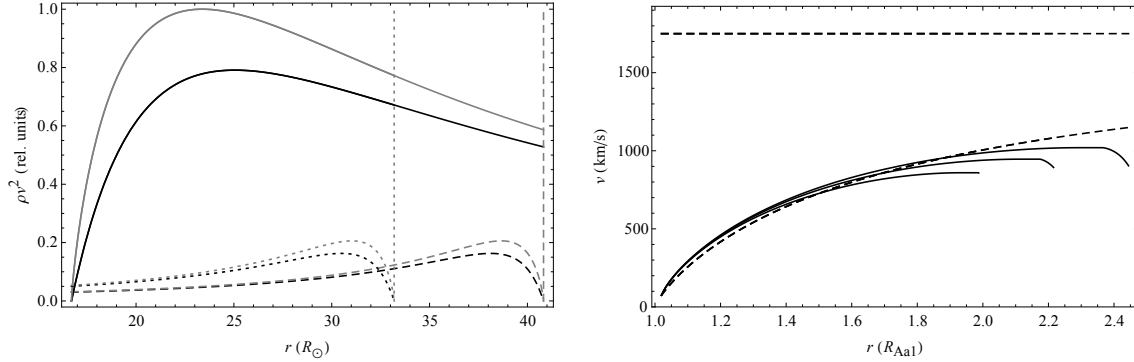


Fig. 9.— Left: Ram pressure of Aa1 (solid) and Aa2 at apastron (dashed) and periastron (dotted). The black lines show a $\beta=1$ law, while the gray lines show a $\beta=0.8$ law. The gray vertical lines represent the location of Aa2’s surface for these two phases. Right: 1D solution to the equation of motion of the primary wind along the line between the stars (solid) at three different separations — apastron (top), semi-major axis (middle), and periastron (bottom). For comparison, the dashed curve shows a $\beta=0.8$ law, and the dashed line shows terminal velocity.

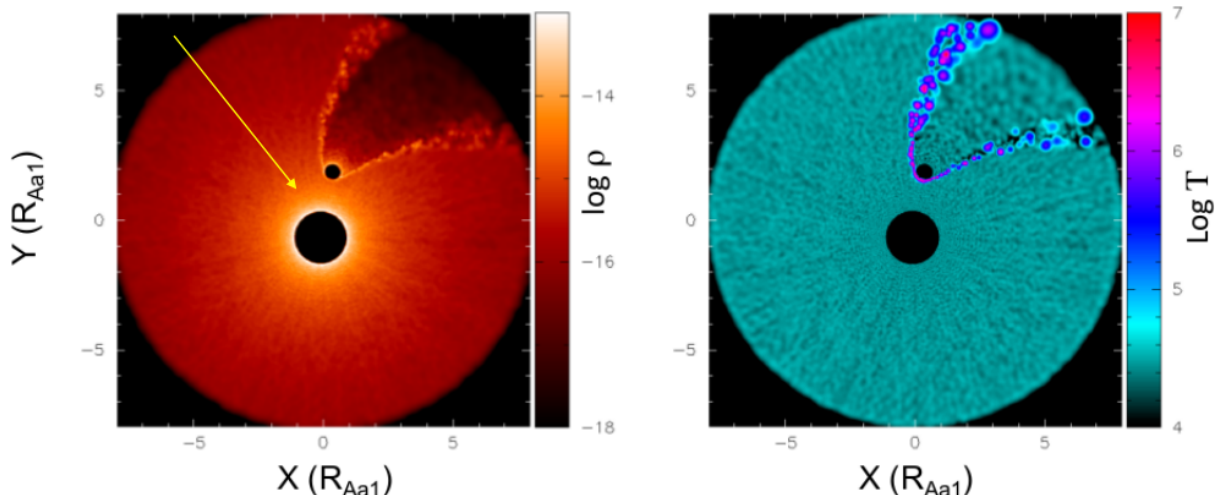


Fig. 10.— Density (left) and temperature (right) structure in the orbital plane from the SPH simulation of δ Ori Aa1 (larger star) and δ Ori Aa2 (smaller star). The arrow shows the orientation of the line of sight. The system is pictured at phase $\phi = 0.87$. The collision of the wind from δ Ori Aa1 against δ Ori Aa2 produces a low-density cavity in the wind of δ Ori Aa1, where the emission from embedded wind shocks is reduced. The collision also produces a layer of hot shocked gas at the boundary of the cavity which produces $< 10\%$ of the emission from the wind shocks embedded in the unperturbed wind from δ Ori Aa1. In the temperature plot on the right, the hot gas from embedded wind shocks in the winds from δ Ori Aa1 and δ Ori Aa2 is ignored, to emphasize the hot gas along the wind collision boundary.

terminal speeds for each star by using the standard reduction in mass-loss rate from the finite disk correction factor, i.e., $\dot{M}_{\text{fd}} = \dot{M}_{\text{CAK}}/(1 + \alpha)^{(1+\alpha)}$. We numerically integrate the equation of motion to distances far from the star to yield the terminal velocity. Then we repeat the process including the radiation and gravity of both stars to determine the speed of each wind along the line between the stars.

Figure 9 shows the equation-of-motion solution for the primary wind. The initial velocity corresponds to a $\beta = 0.8$ law, but radiative inhibition causes the wind (solid) to accelerate less compared to the unmodified β -law (dashed). In addition, the primary wind velocity does begin to decrease from radiative braking. However, Star Aa2’s surface is located at the end of each line, so that the primary wind does not completely stop before it impacts the secondary surface. This indicates that the wind from star Aa1 should still impact the surface of Aa2, even when the influence of the radiation field of star Aa2 is taken into account. Furthermore, due to the strong radiation of Aa1, the wind of Aa2 does not accelerate off the surface of

the star toward Aa1, further suggesting that Aa1’s wind will directly impact Aa2’s surface.

We used a 3D smoothed particle hydrodynamics (SPH) code developed by Benz (1990) and Bate et al. (1995) to model the effects of the wind–wind collision on the extended system wind. Okazaki et al. (2008) was the first to apply this code to a colliding-wind system, and Russell (2013) and Madura et al. (2013) describe the current capabilities of the code, which we briefly state here. The stars are represented as two point masses, and throughout their orbit they inject SPH particles into the simulation volume to represent their stellar winds. The SPH particles are accelerated away from their respective stars according to a $\beta=1$ law (absent from any influence from the companion’s radiation) by invoking a radiative force with a radially varying opacity $\kappa(r)$, i.e. $g_{\text{rad}} = \kappa(r)F/c$, where F is the stellar flux. We take effects of the occultation of one star’s radiation by the other star into account. Radiative inhibition is included in the code (within the context of the radially varying opacity method), but radiative braking is not since it requires the full CAK solution for the wind

driving, which is not yet included in the SPH code. Radiative cooling is implemented via the Exact Integration Scheme (Townsend 2009), and the abundances of both winds are assumed to be solar (Asplund et al. 2009).

The importance of radiative cooling of the shocked material is determined by the parameter $\chi = d_{12}v_8^4/\dot{M}_{-7}$ (Stevens et al. 1992), where d_{12} is the distance to the shock in 10^{12} cm, v_8 is the preshock velocity in 10^8 cm s^{-1} , and \dot{M}_{-7} is the mass-loss rate in $10^{-7} M_\odot \text{ yr}^{-1}$. $\chi > 1$ indicates adiabatic expansion is more important, while $\chi < 1$ indicates that the shocked gas will cool radiatively. For the $\beta=1$ law, χ ranges from $0.5 \lesssim \chi \lesssim 1.3$ between periastron to apastron, so the shocked gas should cool through a combination of adiabatic expansion and radiation.

Figure 10 shows the density and temperature structure of the interacting winds in the orbital plane using the parameters in Table 1. The primary wind impacts the secondary star as expected from the analytical treatment above, where it shocks with newly injected secondary SPH particles. If this interaction leads to SPH particles, either belonging to Aa1 or Aa2, going within the boundary of the secondary star, these particles are accreted, i.e. removed from the simulation. The temperature plot of figure 10 shows that this leads to hot, shocked gas around Aa2, but this must be deemed approximate since the code does not force the Aa1 particles to accrete at the sound speed, which would increase the shock temperature, nor does it include any reflection of Aa1’s radiation off of the surface of Aa2, which would decrease the shock temperature. The half-opening angle is $\sim 30^\circ$, so $\sim 8\%$ of the solid angle of Aa1’s wind is evacuated by Aa2 and its wind.

To determine the X-ray flux from the wind–wind/wind–star collision, we solve the formal solution to radiative transfer along a grid of rays through the SPH simulation volume, for which we use the SPH visualization program **Splash** (Price 2007) as our basis. The emissivity is from the **APEC** model (Smith et al. 2001) obtained from **XSPEC** (Arnaud 1996), the circumstellar material absorbs according to the **windtabs** model (Leutenegger et al. 2010), and the interstellar absorption is from **TBabs** (Wilms et al. 2000b). The radiative transfer calculation is performed at 170 energies logarithmically spaced from 0.2 to 10 keV (100 per dex),

and generates surface brightness maps for each energy. These are then summed to determine the model spectrum, and finally folded through X-ray telescope response functions to directly compare with observations. The overall contamination level of wind–wind/wind–star collision X-rays is $< 10\%$ of the *Chandra* zeroth-order ACIS-S observation, so the influence of emission from shocked gas along the wind–wind boundary is not very significant, though contamination may be larger in some regions of the spectrum, depending on the emission-measure temperature distribution of the colliding-wind X-rays compared to that of the X-rays arising from embedded wind shocks. We caution, however, that the model X-ray flux is dependent on the boundary condition imposed at the surface of Aa2, and so imposing a condition where the incoming wind from star Aa1 shocks more strongly (weakly) will increase (decrease) the amount of X-ray emission from the wind–star collision.

8. Conclusions

Delta Ori Aa is an X-ray bright, nearby, eclipsing binary and so offers the potential to directly probe the X-ray emitting gas distribution in the primary star’s wind as the secondary star revolves through the primary’s wind. Our *Chandra* program was designed to obtain high signal-to-noise and high spectral resolution spectrometry of this system throughout an entire orbit. In this paper, we have sought to characterize the overall spectrum at its highest signal-to-noise ratio by combining all of the *Chandra* spectra and examining temperature distributions and line parameters. Our main results are presented below.

1. Our analysis of the *Chandra* image shows that the emission is mostly dominated by δ Ori Aa, with little detectable emission from δ Ori Ab.
2. The temperature distribution of the X-ray emitting gas can be characterized by three dominant temperatures, which agrees fairly well with the temperature distributions derived by the earlier analysis of Miller et al. (2002) and Raassen & Pollock (2013).
3. The strong lines are generally symmetric, and Gaussian profiles provide a reasonable representation of the profile shape, though

in most cases, and especially for the Ne X and Fe XVII there are significant deviations from Gaussian symmetry.

4. The line widths determined by Gaussian modeling shows that half-widths are typically $0.3-0.5 \times V_\infty$, where V_∞ is the terminal velocity of the wind of δ Ori Aa1. These values are generally larger than the line widths measured by Miller et al. (2002), though it is unclear whether this represents a real change in the line profile or if there is a calibration issue in the analysis of the earlier data set, which was obtained at an anomalously high focal plane temperature.
5. We find a strong anti-correlation between the widths of the H-like and He-like transitions and the excitation energy. This indicates that the lower-energy transitions occur in a region with larger velocities. Assuming a standard wind acceleration law, this correlation probably indicates that the lower-energy lines emerge from further out in the wind.
6. Analysis of strong and weak transitions of Fe XVII and Ne X indicates that resonance scattering may be important in determining the flux and/or shape of the stronger line. This agrees with the analysis of the Fe XVII line by Miller et al. (2002) but at higher significance. We caution that some of these differences in the observed to predicted line ratios may be influenced by an inaccurate temperature distribution and/or uncertainties in the atomic physics. It is also interesting to note that these two lines also have the most non-Gaussian profiles, as shown in Figure 5, perhaps indicative that some line photons have been scattered out of the line of sight.

The spectrum combined from the four individual *Chandra*-HETGS observations represents a very high signal-to-noise view of the emission from δ Ori Aa. However, these observations were obtained at a variety of orbital phases, so that the combined spectrum is a phase-averaged view of the overall X-ray emission from δ Ori Aa. In a companion paper (Nichols et al. 2015) we look for

the effects of phase- and time-dependent changes in the continuum and line spectrum.

We thank the MOST team for the award of observing time for δ Ori A. We also thank our anonymous referee, whose comments significantly improved this paper. M.F.C. would like to thank John Houck and Michael Nowak for many helpful discussions concerning data analysis with ISIS. Support for this work was provided by the National Aeronautics and Space Administration through Chandra Award Number GO3-14015A and GO3-14015E issued by the Chandra X-ray Observatory Center, which is operated by the Smithsonian Astrophysical Observatory for and on behalf of the National Aeronautics Space Administration under contract NAS8-03060. M.F.C., J.S.N., W.L.W., C.M.P.R., and K.H. gratefully acknowledge this support. M.F.C. acknowledges support from NASA under cooperative agreement number NNG06EO90A. N.R.E. is grateful for support from the Chandra X-ray Center NASA Contract NAS8-03060. C.M.P.R. is supported by an appointment to the NASA Postdoctoral Program at the Goddard Space Flight Center, administered by Oak Ridge Associated Universities through a contract with NASA. T.S. is grateful for financial support from the Leibniz Graduate School for Quantitative Spectroscopy in Astrophysics, a joint project of the Leibniz Institute for Astrophysics Potsdam (AIP) and the Institute of Physics and Astronomy of the University of Potsdam. Y.N. acknowledges support from the Fonds National de la Recherche Scientifique (Belgium), the Communauté Française de Belgique, the PRODEX *XMM* and *INTEGRAL* contracts, and the ‘Action de Recherche Concertée’ (CFWB-Académie Wallonie Europe). N.D.R. gratefully acknowledges his CRAQ (Centre de Recherche en Astrophysique du Québec) fellowship. A.F.J.M. is grateful for financial support from NSERC (Canada) and FRQNT (Quebec). J.L.H. acknowledges support from NASA award NNX13AF40G and NSF award AST-0807477. This research has made use of NASA’s Astrophysics Data System. This research has made use of data and/or software provided by the High Energy Astrophysics Science Archive Research Center (HEASARC), which is a service of the Astrophysics Science Division at NASA/GSFC and the High Energy

Astrophysics Division of the Smithsonian Astrophysical Observatory. This research made use of the Chandra Transmission Grating Catalog and archive (<http://tgcat.mit.edu>). The SPH simulations presented in this paper made use of the resources provided by the NASA High-End Computing (HEC) Program through the NASA Advanced Supercomputing (NAS) Division at Ames Research Center.

REFERENCES

- Arnaud, K. A. 1996, in *Astronomical Society of the Pacific Conference Series*, Vol. 101, *Astronomical Data Analysis Software and Systems V*, ed. G. H. Jacoby & J. Barnes, 17
- Asplund, M., Grevesse, N., Sauval, A. J., & Scott, P. 2009, *ARA&A*, 47, 481
- Bate, M. R., Bonnell, I. A., & Price, N. M. 1995, *MNRAS*, 277, 362
- Benz, W. 1990, in *Numerical Modelling of Nonlinear Stellar Pulsations Problems and Prospects*, ed. J. R. Buchler, 269
- Berghoefer, T. W., Schmitt, J. H. M. M., Danner, R., & Cassinelli, J. P. 1997, *A&A*, 322, 167
- Bernitt, S., Brown, G. V., Rudolph, J. K., et al. 2012, *Nature*, 492, 225
- Brinkman, A. C., van Rooijen, J. J., Bleeker, J. A. M., et al. 1987, *Astrophysical Letters and Communications*, 26, 73
- Caballero, J. A., & Solano, E. 2008, *A&A*, 485, 931
- Canizares, C. R., Davis, J. E., Dewey, D., et al. 2005, *PASP*, 117, 1144
- Cantiello, M., Langer, N., Brott, I., et al. 2009, *A&A*, 499, 279
- Cassinelli, J. P., & Swank, J. H. 1983, *ApJ*, 271, 681
- Castor, J. I., Abbott, D. C., & Klein, R. I. 1975, *ApJ*, 195, 157
- Chlebowski, T., Harnden, Jr., F. R., & Sciortino, S. 1989, *ApJ*, 341, 427
- Cohen, D. H., Wollman, E. E., Leutenegger, M. A., et al. 2014, *ArXiv e-prints*, arXiv:1401.7995
- Corcoran, M. F., Waldron, W. L., Macfarlane, J. J., et al. 1994, *ApJ*, 436, L95
- Corcoran, M. F., Nichols, J. S., Pablo, H., et al. 2015, *ArXiv e-prints*, arXiv:1507.05101
- Fisher, P. C., & Meyerott, A. J. 1964, *ApJ*, 139, 123
- Foster, A. R., Ji, L., Smith, R. K., & Brickhouse, N. S. 2012, *ApJ*, 756, 128
- Friend, D. B., & Abbott, D. C. 1986, *ApJ*, 311, 701
- Fruscione, A., McDowell, J. C., Allen, G. E., et al. 2006, in *Society of Photo-Optical Instrumentation Engineers (SPIE) Conference Series*, Vol. 6270, *Society of Photo-Optical Instrumentation Engineers (SPIE) Conference Series*, 1
- Gayley, K. G. 1995, *ApJ*, 454, 410
- Gayley, K. G., Owocki, S. P., & Cranmer, S. R. 1997, *ApJ*, 475, 786
- Gräfener, G., Koesterke, L., & Hamann, W.-R. 2002, *A&A*, 387, 244
- Grant, C. E., Bautz, M. W., Kissel, S. E., LaMarr, B., & Prigozhin, G. Y. 2006, in *Society of Photo-Optical Instrumentation Engineers (SPIE) Conference Series*, Vol. 6276, *Society of Photo-Optical Instrumentation Engineers (SPIE) Conference Series*, 1
- Haberl, F., & White, N. E. 1993, *A&A*, 280, 519
- Hamann, W.-R., & Gräfener, G. 2003, *A&A*, 410, 993
- Harmanec, P., Mayer, P., & Šlechta, M. 2013, in *Massive Stars: From Alpha to Omega*, 70
- Hartmann, J. 1904, *ApJ*, 19, 268
- Harvin, J. A., Gies, D. R., Bagnuolo, Jr., W. G., Penny, L. R., & Thaller, M. L. 2002, *ApJ*, 565, 1216
- Hervé, A., Rauw, G., & Nazé, Y. 2013, *A&A*, 551, A83

- Houck, J. C., & Denicola, L. A. 2000, in *Astronomical Society of the Pacific Conference Series*, Vol. 216, *Astronomical Data Analysis Software and Systems IX*, ed. N. Manset, C. Veillet, & D. Crabtree, 591
- Huenemoerder, D. P., Mitschang, A., Dewey, D., et al. 2011, *AJ*, 141, 129
- Koch, R. H., & Hrivnak, B. J. 1981, *ApJ*, 248, 249
- Kudritzki, R., & Puls, J. 2000, *ARA&A*, 38, 613
- Leutenegger, M. A., Cohen, D. H., Zsargó, J., et al. 2010, *ApJ*, 719, 1767
- Leutenegger, M. A., Paerels, F. B. S., Kahn, S. M., & Cohen, D. H. 2006, *ApJ*, 650, 1096
- Long, K. S., & White, R. L. 1980, *ApJ*, 239, L65
- Lucy, L. B., & White, R. L. 1980, *ApJ*, 241, 300
- Madura, T. I., Gull, T. R., Okazaki, A. T., et al. 2013, *MNRAS*, 436, 3820
- Maíz Apellániz, J., Sota, A., Morrell, N. I., et al. 2013, in *Massive Stars: From alpha to Omega*, 198
- Mayer, P., Harmanec, P., Wolf, M., Božić, H., & Šlechta, M. 2010, *A&A*, 520, A89+
- Miller, N. A., Cassinelli, J. P., Waldron, W. L., MacFarlane, J. J., & Cohen, D. H. 2002, *ApJ*, 577, 951
- Nichols, J. S., Huenemoerder, D. P., Corcoran, M. F., et al. 2015, *ArXiv e-prints*, arXiv:1507.04972
- Okazaki, A. T., Owocki, S. P., Russell, C. M. P., & Corcoran, M. F. 2008, *MNRAS*, 388, L39
- Oskinova, L. M., Feldmeier, A., & Hamann, W.-R. 2006, *MNRAS*, 372, 313
- Owocki, S. P., & Cohen, D. H. 2006, *ApJ*, 648, 565
- Owocki, S. P., Cranmer, S. R., & Gayley, K. G. 1996, *ApJ*, 472, L115+
- Owocki, S. P., & Gayley, K. G. 1995, *ApJ*, 454, L145
- Pablo, H., Richardson, N. D., Moffat, A. F. J., et al. 2015, *ArXiv e-prints*, arXiv:1504.08002
- Pallavicini, R., Golub, L., Rosner, R., et al. 1981, *ApJ*, 248, 279
- Pauldrach, A., Puls, J., & Kudritzki, R. P. 1986, *A&A*, 164, 86
- Price, D. J. 2007, *PASA*, 24, 159
- Raassen, A. J. J., & Pollock, A. M. T. 2013, *A&A*, 550, A55
- Richardson, N. D., Moffat, A. F. J., Gull, T. R., et al. 2015, *ArXiv e-prints*, arXiv:1506.05530
- Russell, C. M. P. 2013, PhD thesis, University of Delaware
- Shenar, T., Oskinova, L., Hamann, W.-R., et al. 2015, *ArXiv e-prints*, arXiv:1503.03476
- Smith, R. K., & Brickhouse, N. S. 2000, in *Revista Mexicana de Astronomia y Astrofisica Conference Series*, Vol. 9, *Revista Mexicana de Astronomia y Astrofisica Conference Series*, ed. S. J. Arthur, N. S. Brickhouse, & J. Franco, 134–136
- Smith, R. K., Brickhouse, N. S., Liedahl, D. A., & Raymond, J. C. 2001, *ApJ*, 556, L91
- Snow, Jr., T. P., Cash, W., & Grady, C. A. 1981, *ApJ*, 244, L19
- Stebbins, J. 1915, *ApJ*, 42, 133
- Stevens, I. R., Blondin, J. M., & Pollock, A. M. T. 1992, *ApJ*, 386, 265
- Stevens, I. R., & Pollock, A. M. T. 1994, *MNRAS*, 269, 226
- Tokovinin, A., Mason, B. D., & Hartkopf, W. I. 2014, *AJ*, 147, 123
- Townsend, R. H. D. 2009, *ApJS*, 181, 391
- Walborn, N. R., Nichols, J. S., & Waldron, W. L. 2009, *ApJ*, 703, 633
- Waldron, W. L., & Cassinelli, J. P. 2001, *ApJ*, 548, L45
- . 2007, *ApJ*, 668, 456
- Walker, G., Matthews, J., Kuschnig, R., et al. 2003, *PASP*, 115, 1023

Wilms, J., Allen, A., & McCray, R. 2000a, ApJ,
542, 914

—. 2000b, ApJ, 542, 914